Investigating the Design Space for Solar Sail Trajectories in the Earth-Moon System

Geoffrey G. Wawrzyniak* and Kathleen C. Howell*

School of Aeronautics and Astronautics, Purdue University, West Lafayette, IN 47906, USA

Abstract: Solar sailing is an enabling technology for many mission applications. One potential application is the use of a sail as a communications relay for a base at the lunar south pole. A survey of the design space for a solar sail spacecraft that orbits in view of the lunar south pole at all times demonstrates that trajectory options are available for sails with characteristic acceleration values of 1.3 mm/s^2 or higher. Although the current sail technology is presently not at this level, this survey reveals the minimum acceleration values that are required for sail technology to facilitate the lunar south pole application. This information is also useful for potential hybrid solar-sail-low-thrust designs. Other critical metrics for mission design and trajectory selection are also examined, such as body torques that are required to articulate the vehicle orientation, sail pitch angles throughout the orbit, and trajectory characteristics that would impact the design of the lunar base. This analysis and the techniques that support it supply an understanding of the design space for solar sails and their trajectories in the Earth-Moon system.

Keywords: Solar sail, design space, survey, lunar south pole, communications relay.

1. INTRODUCTION

In 2004, the Vision for Space Exploration directed NASA to establish an outpost at the lunar south pole (LSP) [1] by 2020. While this goal has since been revised, the announcement of such a potential outpost motivated studies for establishing a communications architecture to support mission personnel [2]. Because line-of-sight transmission to the Earth (or to a relay in LEO) is not guaranteed at the LSP, multiple spacecraft in Keplerian orbits about the Moon are necessary to serve as communications relays [3-5]. Exotic solutions that exploit halo orbits about the cis- and trans-lunar Lagrange points have also been examined [6].

A novel approach to this LSP-coverage problem is a single spacecraft in a trajectory that places the spacecraft in view of the LSP and the Earth at all times. This approach requires an additional force on the spacecraft. One concept for using a single vehicle to maintain coverage employs an an NSTAR low-thrust engine [7,8]. In this scenario, a spacecraft of 500 kg mass spirals out from LEO to a fuel-optimal orbit below the trans-lunar Lagrange point. Alternatively, a solar sail spacecraft can also supply the requisite additional force for an orbit to remain in view of the LSP [9,10]. In ref. [9], a 235-255 kg spacecraft completes a conventional transfer from the Earth to a lunar orbit. Once in orbit, a solar sail with a characteristic acceleration of up to 1.338 mm/s^2 ("a modest improvement in contemporary solar sail technology" [9]) is deployed and used to maintain the spacecraft below the trans-lunar Lagrange point. A carrier vehicle is jettisoned and the mass of the remaining vehicle is 195 kg. A third strategy combines solar sails and low-thrust, solar-electric propulsion into a hybrid system to deliver the vehicle into an orbit that remains in view of the LSP at all times [11].

The design space for these single-spacecraft solar sail missions is not well known. Advances in computing power have made extensive surveys of various design spaces for spacecraft trajectories possible in recent years [12-15]. The present investigation employs a survey technique to examine the design trade space for a solar sail in the Earth-Moon system. Similar to previous work by the authors [15], multiple grids of initial guesses are created and then used to initialize a numerical solution technique for boundary-value problems that generates feasible trajectory options. The initial guesses are distinguished by the size and shape of the guessed path as well as the nominal control history that is required to maintain the path. Both the path and control profile are modified by the boundary-value problem (BVP) solver. Solutions are examined for different spacecraft and mission performance metrics. A characteristic acceleration of 1.7 mm/s^2 is employed to demonstrate the survey techniques when critical metrics other than characteristic acceleration are examined. These techniques may be applied to sails possessing other, more realistic, characteristic accelerations or spacecraft employing other propulsion devices (e.g., low-thrust, electric sails, hybrid systems) in future investigations.

Beginning with a description of the LSP problem, a brief discussion of possible numerical techniques for solving BVPs ensues. Construction of the design space includes the initial guess combinations employed in the survey; the critical metrics for evaluation of the feasible LSP-coverage orbits from the survey are examined.

2. SYSTEM MODELS AND CONSTRAINTS

The LSP-coverage problem requires that a spacecraft be in contact with a facility at the lunar south pole at all times.

*Address correspondence to these authors at the School of Aeronautics and Astronautics, Purdue University, West Lafayette, IN 47906, USA;
Tel: (765) 494-7896; Fax: (765) 494-0307;
E-mails: gwawrzyn@purdue.edu, howell@purdue.edu

1874-1460/11

The Earth and the Moon can be considered a binary system, and thus it is beneficial to model the motion of the solar sail spacecraft within the context of a circular restricted three-body model. Path constraints are incorporated such that the sail remain in view of the LSP throughout one period of its orbit. Finally, the ability to control the trajectory of the spacecraft is coupled to the orientation of the sail. Spacecraft body rotations, along with system models and constraints are examined in the following subsections.

2.1. Dynamical Model

The LSP-coverage problem is defined within the context of the circular restricted three-body (CR3B) system, that is, the problem is formulated in a frame, R, that is rotating with respect to an inertial system, I. A CR3B model that incorporates the gravity contributions of two primary bodies is geometrically advantageous for understanding the problem. Consistent with McInnes [16], the nondimensional vector equation of motion for a spacecraft at a location $\mathbf{r}$ relative to the barycenter (center of mass of the primaries) is

$$ {}^{R}\mathbf{a} + 2\left({}^{I}\omega^{R} \times {}^{R}\mathbf{v}\right) + \nabla U(\mathbf{r}) = \mathbf{a}_s(t) \tag{1}$$

where the first term is the acceleration relative to the rotating frame (more precisely expressed as $\frac{{}^{R}d^2\mathbf{r}}{dt^2}$, where the left superscript R indicates a derivative in the rotating frame) and the second term is the corresponding Coriolis acceleration, which requires the velocity relative to the rotating frame, ${}^{R}\mathbf{v}$ (more precisely $\frac{{}^{R}d\mathbf{r}}{dt}$).[1] The position and velocity vectors are

$$\mathbf{r} = \left\{ \begin{array}{ccc} x & y & z \end{array} \right\}^{\mathrm{T}} \tag{2}$$

$$\mathbf{v} = \left\{ \begin{array}{ccc} \dot{x} & \dot{y} & \dot{z} \end{array} \right\}^{\mathrm{T}} \tag{3}$$

where the superscript R indicating a velocity relative to the rotating frame has been dropped for convenience. The angular-velocity vector, ${}^{I}\omega^{R}$, relates the rate of change of the rotating frame with respect to the inertial frame. The applied acceleration, from a solar sail in this case, is indicated on the right side by $\mathbf{a}_s(t)$. The pseudo-gravity gradient, $\nabla U(\mathbf{r})$, combines the centripetal and gravitational accelerations

$$\nabla U(\mathbf{r}) = \left({}^{I}\omega^{R} \times \left({}^{I}\omega^{R} \times \mathbf{r}\right)\right) + \left(\frac{(1-\mu)}{r_1^3}\mathbf{r}_1 + \frac{\mu}{r_2^3}\mathbf{r}_2 \right) \tag{4}$$

where μ represents the mass fraction of the smaller body, or $m_2/(m_1+m_2)$, and r_1 and r_2 are the distances from the larger and smaller bodies, respectively, that is,

$$\mathbf{r}_1 = \sqrt{(\mu + x)^2 + y^2 + z^2}$$

$$\mathbf{r}_2 = \sqrt{(\mu + x - 1)^2 + y^2 + z^2}$$

Solar gravity is neglected in this model. At a distance of 1 AU, an appropriate assumption for a sailcraft in the Earth-Moon system, the applied acceleration from a solar sail is modeled as

$$\mathbf{a}_s(t) = \beta(\hat{\ell}(t) \cdot \hat{\mathbf{u}})^2 \hat{\mathbf{u}} \tag{5}$$

where u is the sail-face normal, $\hat{\ell}(t)$ is a unit vector in the Sun-to-spacecraft direction, and β is the sail's characteristic acceleration in nondimensional units. Note that sail acceleration is always assumed to be normal to the sail face. These vectors appear in Fig. (**1**).

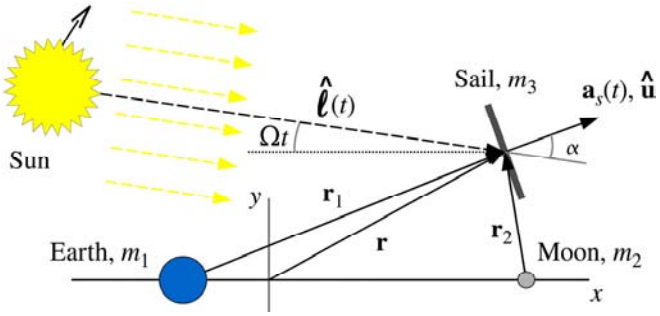

Fig. (1). Earth-Moon system model.

Observed from the rotating frame, R, the Sun moves in a clockwise direction about the fixed primaries. The sail mass, m_3, is negligible compared to the masses of the Earth and Moon, which are m_1 and m_2, respectively. The term $(\hat{\ell}(t) \cdot \hat{\mathbf{u}})$ is also expressed as $\cos\alpha$, where α is the sail pitch angle, or the angle between the solar incidence direction and the sail-face normal.

To generate the magnitude of the sail acceleration in dimensional units, a_0, β is multiplied by the system characteristic acceleration, a^*, which is the relationship between the dimensional and nondimensional acceleration in Eq. (1). In fact, a^* is the ratio of the characteristic length, L^* (384,400 km for the Earth-Moon distance), to the square of the characteristic time, t^* ($2\pi t^* = 27.321$ days), that is,

$$a^* = \frac{L^*}{(t^*)^2} = 2.7307 \text{ mm/s}^2$$

The sail modeled here is a perfectly reflecting, flat solar sail. Higher fidelity models include optical models [16], parametric models that incorporate billowing in addition to optical effects [16,17], and realistic models based on finite-element analysis that incorporates optical properties and manufacturing flaws [18]. Optical effects represent a non-perfectly reflecting solar sail; some energy is absorbed, and some is reflected diffusely as well as specularly. An ideal sail reflects only specularly. In all of these higher-fidelity models, the resulting acceleration from a solar sail is not perfectly parallel to the sail-face normal but, instead, is

[1]Vectors are denoted with boldface. Derivatives of the position vector (${}^{R}\mathbf{v}$ and ${}^{R}\mathbf{a}$) are assumed to be relative to the rotating frame and, consequently, R is dropped.

increasingly offset from the sail-face normal as the sail is pitched further from the sunlight direction [16]. Nevertheless, this analysis employs an ideal sail to lend insight into the technology level required to solve the LSP-coverage problem.

2.2. Constraint Models

One physical constraint is imposed on the attitude of the spacecraft: the sail-face normal, $\hat{\mathbf{u}}$, which is coincident with the direction of the resultant force in an ideal model, is always directed away from the Sun. This constraint is written mathematically as

$$\hat{\ell}(t) \cdot \hat{\mathbf{u}} \geq \cos \alpha_{\max} \tag{6}$$

where $\alpha_{\max}$ is 90°. Recall that the sail modeled here is perfectly reflecting and flat. Billowing is not incorporated in this force model; however, $\alpha_{\max}$ can be less than 90°, as sail luffing (i.e., flapping) is assumed to occur at high pitch angles [19]. Fully incorporating realistic solar sail properties attenuates the sail characteristic acceleration by nearly 25% and places an upper limit on the pitch angle between 50° and 60° for sail effectiveness, depending on the properties of the sail [18].

In this analysis, an elevation-angle constraint, $E_{\min}$, maintains the visibility of the spacecraft from a location near the south pole of the Moon, and a spacecraft altitude constraint, $A_{\max}$, is imposed such that solutions remain within the vicinity of the Moon and do not escape to a region about the combined Earth-Moon system. Altitude is defined as the distance from the lunar south pole, that is,

$$A = \sqrt{(x-1+\mu)^2 + y^2 + (z+R_m)^2} \tag{7}$$

where R_m is the lunar radius (approximately 1737 km). A third path constraint requires that the sail-face normal, or control $\hat{\mathbf{u}}$, is always directed away from the Sun (the sunlight vector is $\hat{\ell}$), or $\alpha_{\max} = 90^\circ$ in Eq. (6). Of the inequality constraints, only this attitude requirement is mandated. In addition to the constraint in Eq. (6), the inequality path constraints are

$$E_{\min} \leq E \equiv \arcsin\left(-\frac{z+R_m}{A}\right) \tag{8}$$

$$A_{\max} \geq A \tag{9}$$

For the given problem and model, adding a path constraint to avoid the penumbra and umbra of the Earth or the Moon shadow is unnecessary because of the elevation-angle constraint. A shadow constraint could be added for another application or shadowing effects could be directly incorporated into the dynamical model [20]. Additional inequality path constraints could include limits on the body turn rates and the accelerations governed by the attitude control system of the spacecraft. Note that these path constraints are identical to those appearing in refs. [15,21]. The two path constraints in Eqs. (8) and (9), as well as a periodicity constraint, are illustrated in Fig. (**2**). The attitude constraint from Eq. (6) appears in Fig. (**1**). The sailcraft in Fig. (**2**) orbits below the Moon. Feasible solutions also exist that do not cycle below the Moon, but rather below either the L_1 or the L_2 point.

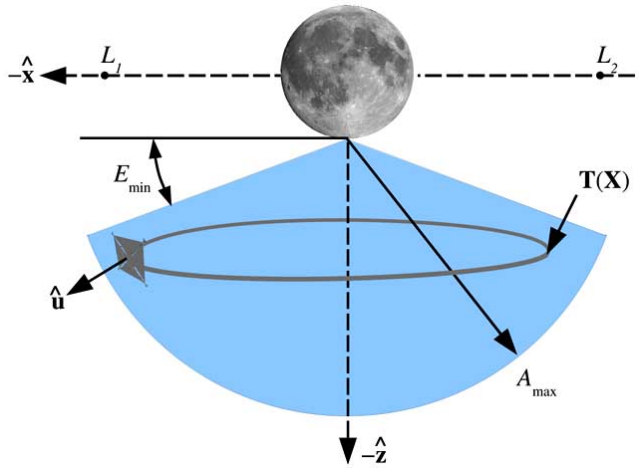

Fig. (2). Path constraints for an orbit below the Moon (Moon image from nasa.gov).

Periodic solutions exist for a sailcraft within the context of a two- or three-body regime. When more primaries are included in the dynamical model, especially if the dynamical model is based on positions of the primaries from a planetary ephemeris, a periodic solution may not be available and a quasi-periodic solution must suffice. In this event, a solution from the lower-fidelity two- or three-body system is used to initialize a numerical process that does not constrain periodicity [10].

2.3. Sail Orientation Model

A series of rotations is employed to transform a vector from a sailcraft body-fixed frame to the inertial frame [22]. These rotations aid in expressing the angular velocity vector of the body-fixed frame with respect to the inertial frame, ${}^I\omega^B$. A variety of rotation sequences are enlisted to describe these rotations, however, it is useful to develop ${}^I\omega^B$ based on existing orientation angles, such as α, δ, and Ωt (pitch, clock, and sunlight angle, respectively). This analysis assumes that the Sun's rays are parallel at 1 AU and that the Sun moves in a circle about the Earth-Moon barycenter as well as in the Earth-Moon orbit plane.

The first step in transforming from the inertial frame to a body-fixed frame is an initial transformation from the inertial frame, I, to a solar frame, F, where $\hat{\mathbf{x}}'$ is aligned with $\hat{\ell}$, as evident in Fig. (**3**). Because the rotating frame R is moving counterclockwise about a common $\hat{\mathbf{z}}$ axis with respect to the inertial frame and the Sun is moving clockwise about the same $\hat{\mathbf{z}}$ axis at a rate of Ω, the first two rotations are consolidated into a single rotation about the $\hat{\mathbf{z}}$ axis of

$$\begin{Bmatrix} \hat{\mathbf{x}}' \\ \hat{\mathbf{y}}' \\ \hat{\mathbf{z}}' \end{Bmatrix} = {}^F T_3^I(t-\Omega t) \begin{Bmatrix} \hat{\mathbf{X}} \\ \hat{\mathbf{Y}} \\ \hat{\mathbf{Z}} \end{Bmatrix} \tag{10}$$

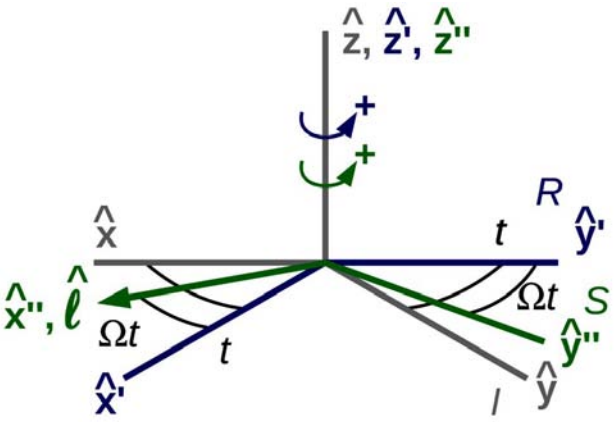

Fig. (3). Rotations from the inertial frame, I, to the solar frame, F, *via* the Earth-Moon rotating frame, R.

$$ {}^{F}T_{3}^{I}\left(t-\Omega t\right)=\begin{bmatrix} \cos(t-\Omega t) & \sin(t-\Omega t) & 0 \\ -\sin(t-\Omega t) & \cos(t-\Omega t) & 0 \\ 0 & 0 & 1 \end{bmatrix} \tag{11} $$

The sail-face normal in the Sun-fixed frame, F, is expressed in terms of α and δ

$$ \hat{\mathbf{u}}=\begin{Bmatrix} \cos\alpha \\ \sin\delta\sin\alpha \\ \cos\delta\sin\alpha \end{Bmatrix} \tag{12} $$

where δ is also known as the clock angle and is measured about the sunline, $\hat{\ell}$, from the $\hat{\mathbf{z}}$ axis in the R frame, as illustrated in Fig. (**4**).

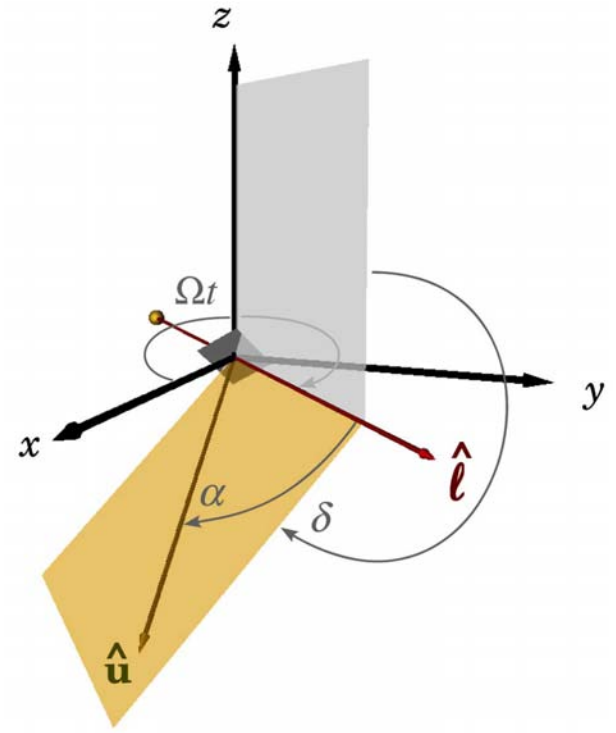

Fig. (4). Pitch, α, and clock, δ, angles for the sail-face normal with respect to the sunline. The axes are fixed in the rotating frame and the Sun moves about the Earth-Moon system at a rate of Ω.

The sunlight direction is expressed relative to the rotating frame, R (the same frame in which the vector equations of motion, Eq. (1), are formulated), and is a function of time, that is,

$$ \hat{\ell}(t)=\cos(\Omega t)\hat{\mathbf{x}}-\sin(\Omega t)\hat{\mathbf{y}}+0\hat{\mathbf{z}} \tag{13} $$

where Ω is the ratio of the synodic rate of the Sun as it moves along its path to the system rate, approximately 0.9192. The sunlight direction in the Earth-Moon system appears in Figs. (**1**, **4**). Expressing $\hat{\mathbf{u}}$ in the working frame, R, requires a rotation of $\hat{\mathbf{u}}$ by $-\Omega t$ about the $\hat{\mathbf{z}}$ axis.

The next set of rotations transforms the axes from the solar frame, F, to a frame on, but not rotating with, the sailcraft, denoted the C frame. The coordinate frame is rotated through the clock angle, δ, about the $\hat{\mathbf{x}}'$ axis, then by the pitch angle, α, about the $\hat{\mathbf{y}}''$ axis, as defined in Fig. (**5**). The associated transformation equations are

$$ \begin{Bmatrix} \hat{\mathbf{x}}''' \\ \hat{\mathbf{y}}''' \\ \hat{\mathbf{z}}''' \end{Bmatrix}={}^{S}T_{2}^{D}(-\alpha)^{D}T_{1}^{F}(-\delta)\begin{Bmatrix} \hat{\mathbf{x}}' \\ \hat{\mathbf{y}}' \\ \hat{\mathbf{z}}' \end{Bmatrix} \tag{14} $$

$$ {}^{S}T_{2}^{D}\left(-\alpha\right)^{D}T_{1}^{F}\left(-\delta\right)=\begin{bmatrix} \cos\alpha & \sin\alpha\sin\delta & \cos\delta\sin\alpha \\ 0 & \cos\delta & -\sin\delta \\ -\sin\alpha & \cos\alpha\sin\delta & \cos\alpha\cos\delta \end{bmatrix} \tag{15} $$

The matrix in Eq. (15) can be combined with the maxtrix in Eq. (12).

A final rotation is required to transform from the C frame to a body-fixed frame, S, *via* θ about the sail-face normal, $\hat{\mathbf{u}}$, as indicated in Fig. (**6**). Note that $\dot{\theta}$ is the relative rotation rate and not the spin rate [22]. If the spin rate is fixed, the relative rotation angle is a function of the spin rate and other angular terms. The associated transformation equations are

$$ \begin{Bmatrix} \hat{\mathbf{x}}^{iv} \\ \hat{\mathbf{y}}^{iv} \\ \hat{\mathbf{z}}^{iv} \end{Bmatrix}={}^{S}T_{1}^{C}\left(\theta\right)\begin{Bmatrix} \hat{\mathbf{x}}''' \\ \hat{\mathbf{y}}''' \\ \hat{\mathbf{z}}''' \end{Bmatrix} \tag{16} $$

$$ {}^{S}T_{1}^{C}\left(\theta\right)=\begin{bmatrix} 1 & 0 & 0 \\ 0 & \cos\theta & \sin\theta \\ 0 & -\sin\theta & \cos\theta \end{bmatrix} \tag{17} $$

A full rotation from the inertial frame to the body frame is

$$ {}^{S}T^{I}={}^{S}T_{1}^{C}(\theta)^{C}T_{2}^{D}(-\alpha)^{D}T_{1}^{F}(-\delta)^{F}T_{3}^{R}(-\Omega t)^{R}T_{3}^{I}(t) \tag{18} $$

The above rotations are employed to formulate the angular velocity vector. The angular velocity vector, ${}^{I}\omega^{S}$, is constructed from the angular velocities of each rotation, that is,

$$ {}^{I}\omega^{S}={}^{I}\omega^{F}+{}^{F}\omega^{D}+{}^{D}\omega^{C}+{}^{C}\omega^{S} \tag{19} $$

$$ =(1-\Omega)\hat{\mathbf{z}}'-\dot{\delta}\hat{\mathbf{x}}''-\dot{\alpha}\hat{\mathbf{y}}'''+\dot{\theta}\hat{\mathbf{x}}^{iv} \tag{20} $$

When expressed in body-fixed coordinates,

(**a**) S frame to D frame (**b**) D frame to C frame

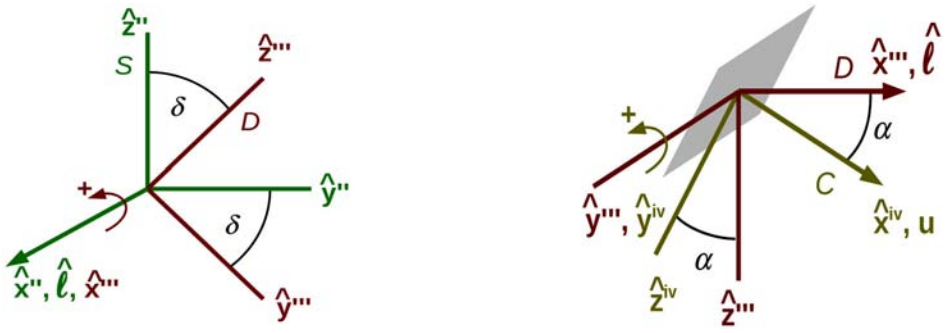

Fig. (5). Rotation from the solar frame, S, to the sailcraft frame, C, *via* an intermediate frame, D.

$$ {}^{I}\omega^{S} = \begin{Bmatrix} \dot{\theta} - \dot{\delta}\cos\alpha + (1-\Omega)\sin\alpha\cos\delta \\ -\dot{\alpha}\cos\theta + \dot{\delta}\sin\theta\sin\alpha + (1-\Omega)(\sin\theta\cos\alpha\cos\delta - \cos\theta\sin\delta) \\ \dot{\alpha}\sin\theta + \dot{\delta}\cos\theta\sin\alpha + (1-\Omega)(\cos\theta\cos\alpha\cos\delta + \sin\theta\sin\delta) \end{Bmatrix} \quad (21) $$

If the spacecraft possesses a fixed spin rate, whether it is three axis stabilized ($\omega_{x0} = 0$) or spinning ($\omega_{x0} \neq 0$), the relative rotation angle, θ, is integrated from

$$ \dot{\theta} = \omega_{x0} + \dot{\delta}\cos\alpha + (1-\Omega)\sin\alpha\cos\delta \quad (22) $$

Finally, because the angular velocity vector is expressed in terms of the body-fixed frame, a derivative of Eq. (21) is required to determine the angular acceleration vector, ${}^{I}\dot{\omega}^{S}$; a central-difference approximation of ${}^{I}\omega^{S}$ is sufficient. Both the angular velocity and the angular acceleration are required to calculate the specific transverse torque, described in Section 4.2.1, that is required to physically reorient the sailcraft.

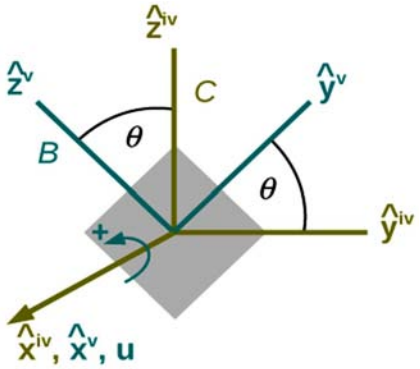

Fig. (6). Rotations from the C frame to the body-fixed frame, S.

3. NUMERICAL BVP SOLVERS

Adapting numerical processes to solve boundary-value problems (BVPs) is advantageous. A trajectory is a set of states that satisfies a set of equations of motion (EOMs). The EOMs are often formulated as ordinary differential equations (ODEs). If a state along a path is known at a specific time, then solving for the entire path can be cast as an initial-value problem and propagated using explicit- or implicit-integration methods. If path constraints exist along a trajectory, numerical techniques for solving BVPs are employed. Because the attitude is dynamically tied to the trajectory for the solar sail problem, an algorithm for generating a nominal path must also return an associated control profile.

Some common numerical procedures for solving BVPs include single and multiple shooting, collocation, and finite-difference methods [21,23-25]. For the present study, two augmented finite-difference methods, described in Wawrzyniak and Howell [21], are employed to survey the design space for solar sails in orbits offset below the lunar south pole. Both methods return a nominal trajectory and associated control profile.

Four sample orbits, generated from an augmented finite-difference approach, appear in Fig. (**7**). The arrows directed away from points along the trajectory indicate the direction of the sail-face normal, $\hat{\mathbf{u}}$, and are separated in time by approximately one day. The Moon is plotted to scale. The path in each of these four solutions originates on the L_2 side of the Moon, in a location indicated by an "x," and move on a clockwise (retrograde) path. In this Earth-Moon frame, the Sun is initially aligned with the $-x$ axis, but moves clockwise about the Earth-Moon system with a period of one sidereal month (29.5 days); not coincidentally, the sailcraft trajectories possess the same period. Note that each of these orbits meets the constraints established in Section 2.2.

The associated control profiles of the four sample orbits in Fig. (**7**) appear in Fig. (**8**). Of these four trajectories, the light-blue path under the Moon requires the smallest maximum pitch angle, α, and the orange path under the Moon is associated with the highest maximum pitch angle. These maximum angles occur on the right side ($+x$ side) of the light-blue orbit in Fig. (**7**), when the Sun is initially positioned along the $-x$ axis (at day 0 in Fig. **8**). The maximum pitch angle associated with the orange orbit occurs when the spacecraft is near the extremities in the $\pm y$ directions of that trajectory (at days 9 and 20 in Fig. **8**).

4. SURVEY OF THE DESIGN SPACE

The solution space, also known as the search space or feasible region, is one that meets all problem constraints and includes all candidate solutions. The feasible region contains one or more locally optimal solution and many other sub-optimal solutions. For traditional spacecraft that rely on chemical or electric propulsion, the cost that must be

(**a**) Side view, *xz* (**b**) 3D view

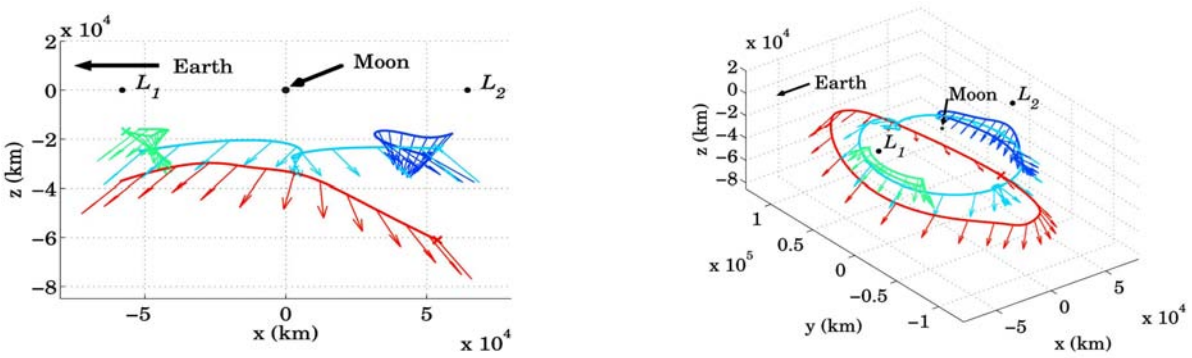

Fig. (7). Four sample orbits generated from an augmented finite-difference method.

optimized is almost always propellant (or spacecraft mass). However, optimal solutions are often adjusted to accommodate spacecraft- and mission-design considerations not addressed when posing the original optimization problem. Examples include "soft" considerations such as the relative merits of one scientific plan or one operational strategy versus another.

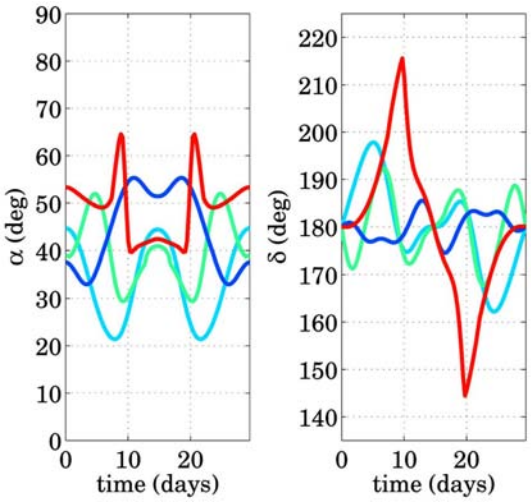

Fig. (8). Associated control profiles corresponding to the orbits in Fig. (**7**).

Complex optimization problems with a plethora of locally optimal solutions require good initial guesses to seed their respective numerical-solution algorithms. If the solution space in general is known, an appropriate initial design is selected for further refinement. The solution space for the LSP coverage problem is not well understood for solar sails. Similar problems have been examined through analytical approaches [11,26] as well as numerical techniques [10,27]. However, the design space for the LSP coverage problem remains relatively unexplored. A numerical survey is a reasonable strategy to gain insight into this problem, whereby a large set of initial guesses for potential periodic solutions is used to initialize a numerical process [15]. The results are collected and searched for trajectories characterized by desirable features. A variety of initial guess combinations are investigated for the path, the nominal attitude profile, and the sail characteristic acceleration.

4.1. Initial Guess Combinations

Not surprisingly, the initial guesses for the trajectory and the control history influence the resulting solution. Two types of initial guesses are explored for the path, as well as six different types for the initial guess corresponding to the control history. The various combinations are summarized in Table **1**. The superscript "0" indicates an initial guess for the associated variable.

4.1.1. Initial Guesses for the Trajectory

Circular orbits Due to the required periodicity of the converged solution, co-axial circles offset from the Moon in the z direction are selected as one option for an orbit to develop the initial guess: the x and y coordinates are defined by simple sinusoidal functions moving in a retrograde fashion and the z components are constant (cases labeled "Cr" in Table **1**). For a retrograde orbit about the Moon, the spacecraft and the Sun are in opposition throughout the cycle. For a prograde orbit, the spacecraft is initially located between the Sun and the Moon, but moves counter-clockwise as the Sun moves clockwise about the Moon as viewed in the rotating frame (cases labeled "Cp" in Table **1**). Associated initial guess velocities are defined as the time derivatives of these sinusoidal functions. In some cases, the converged trajectories appear similar to their respective offset luni-axial circles; in most trials, however, the converged solution does not resemble the initial circle.

Static point The other possible option for the development of an initial guess for the trajectory is simply a static point, located initially in the xz plane as defined for the Earth-Moon CR3B system. This option is denoted as "P" in Table **1**. Of course, only the two Lagrange points near the Moon preserve this initial guess as a converged result, and only for certain conditions: (1) if any constraint on elevation that might exist allows for it and (2) if the sail-face normal is orthogonal to the sunline, or "off," at all times. Nevertheless, the augmented finite-difference methods, developed by Wawrzyniak and Howell [21], converge on many different periodic solutions using this "P" strategy.

Four initial guesses for the path are illustrated in Fig. (**9**). Two initial guesses are circles, axially offset from the center of the Moon, and the two others are static-point initial

Table 1. Summary of Initial Guess Strategies for the Trajectory and Control History

IG* Trajectory	IG Control	Description
Cr		$\mathbf{r}^0$ is a retrograde circle, offset from Moon in $-z$ direction
Cp		$\mathbf{r}^0$ is a prograde circle, offset from Moon in . $-z$. direction
P		$\mathbf{r}^0$ clustered at a point near the Moon in southern xz half-plane
	α^*	$\hat{\mathbf{u}}_i^0$ south from Sun-line by 35.26°
	Moon	$\hat{\mathbf{u}}_i^0$ away from Moon
	EOM-NR	$\mathbf{u}_i^0$ satisfies EOM at each epoch, $\|\mathbf{u}_i^0\|$ not necessarily equal to 1
	RAA	$\hat{\mathbf{u}}_i^0$ is in direction of required applied acceleration at each epoch
	∇U	$\hat{\mathbf{u}}_i^0$ points in the direction of $\nabla U(\mathbf{r}(t_i))$
	$\hat{\ell}$	$\hat{\mathbf{u}}_i^0$ points along the sunline, $\hat{\ell}(t_i)$

*IG: Initial Guess.

guesses below L_1 and L_2. These circles and points are used as initial guesses for the sample orbits in Fig. (**7**). The xz plane below the Moon can be populated with initial guesses, potentially incorporated into a large simulation. In this analysis, for trials in which the initial trajectory guess is a point and in the xz plane, a grid spanning -75000 to 75000 km in the x direction and -75000 to 0 km in the z direction, each in 1000 km increments are used to generate the initial values, x^0 and z^0, for all points along the path. When the initial guess for the path is a concentric circle below the Moon, a grid of radii and z-offset values span a region from 0 to 75000 km and -75000 to 0 km, respectively, in 1000 km increments.

Initial guess strategies where the circular orbit possesses a period of one half the synodic period or twice the synodic period are cursorily examined. Strategies to deliver circular orbits with periods half the synodic period of $2\pi/\Omega$ do not result in solutions with periods of π/Ω (i.e., two revolutions of the orbit per synodic cycle). When employing circular initial guesses with an initial period of $4\pi/\Omega$, the time frame of the simulation is extended to $[0, 4\pi/\Omega]$, allowing the Sun to make two revolutions about the system while the spacecraft completes one revolution.

Three types of solutions are observed when the simulation time is extended to twice the synodic period. (1) The first is where an orbit possessing a period of $2\pi/\Omega$ is simply repeated. The second and third type are actually two forms of a single-revolution solution. (2) In the second type, the path initially appears to be centered in a region below L_1, the Moon or L_2. After $t = \pi/\Omega$, the path shifts to a different region, and then after $t = 3\pi/\Omega$, the path returns to the original region. A sample orbit illustrating this phenomenon appears in red in Fig. (**10**). Originating at the red "x" below L_2, the spacecraft moves along the path in a clockwise direction. The center of the path shifts to a region under L_1 when $t = \pi/\Omega$ and the Sun is located along the $+x$ axis. The motion after $t = 2\pi/\Omega$ mirrors the motion before that time. (3) The third type of solution behaves similar to the second, except that the center of the path remains under the same location. The orange orbit in Fig. (**10**) exhibits this behavior. For both of these sample orbits, the initial spacecraft motion is in the $-y$ direction (recall that the Sun initially moves in the $+y$ direction and completes one clockwise revolution about the system during the synodic period of $2\pi/\Omega$).

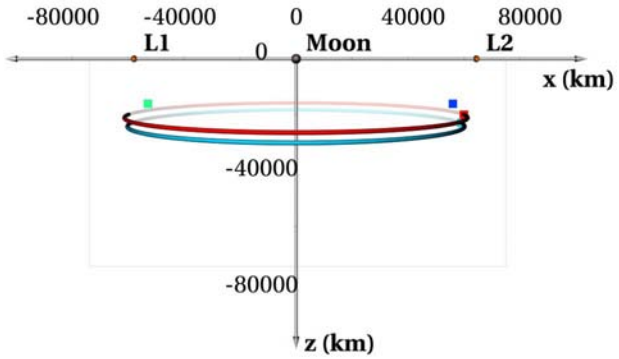

Fig. (9). Four sample initial guesses for the path. The origin of the coordinate system is the center of the Moon.

These multiple-revolution solutions demonstrates both their existence and that the augmented finite-difference methods by Wawrzyniak and Howell [21] can generate trajectories with time spans longer than one synodic period. Because the sample space already exceeds 10 million combinations of initial guesses where the path is a circle with a period of $2\pi/\Omega$, initial guesses where the path is initially a circle with a period of some multiple of $2\pi/\Omega$ are not included in this investigation.

4.1.2. Initial Guesses for the Control History

The "control history" refers to the direction of the sail-face normal, or applied thrust vector; the control directions are initially defined at discrete points along the entire orbit. Six concepts are explored as potential initial guesses for the control history (producing a total of twelve combined initial guess strategies).

An optimal attitude: "α^*" The first control strategy simply maximizes the out-of-plane force contributed by the sail ("α^*" in Table **1**). Derived analytically by McInnes

(**a**) Top view, *xy* (**b**) Side view, *xz*

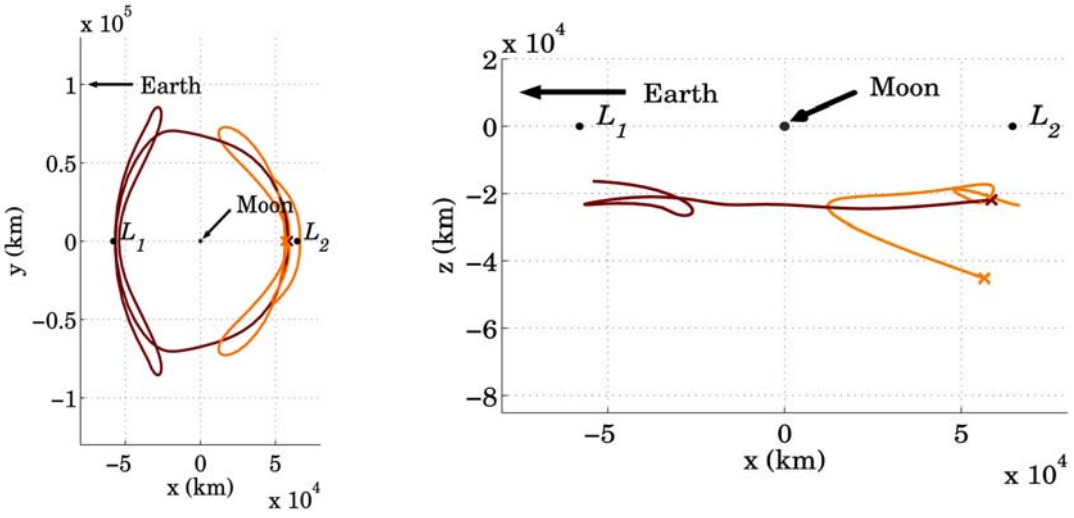

Fig. (10). Sample double orbits. Note that the initial guesses for these orbits are circular paths that have periods twice that of the synodic period.

[16], the sail-pitch angle that maximizes the out-of-plane thrust is $\alpha^* = 35.26^\circ$. The initial guess for the thrust vector is then

$$\hat{\mathbf{u}}_i^0 = \cos(\Omega t_i)\cos\alpha^*\hat{\mathbf{x}} - \sin(\Omega t_i)\cos\alpha^*\hat{\mathbf{y}} + \sin\alpha^*\hat{\mathbf{z}} \tag{23}$$

This initial guess for the control strategy, combined with a static-point-type initial guess for the trajectory, is very successfully applied by Ozimek *et al*. [10].

Sail-face normal directed away from the Moon: "Moon" The next strategy that serves as an initial guess option for the control is a thrust vector directed away from the center of the Moon throughout the initial guess trajectory ("Moon" in Table **1**). Thus, if a vector, $\mathbf{r}_i^c$, is defined as the difference between the position of the Moon and the position of the spacecraft in the rotating frame at time t_i, or

$$\mathbf{r}_i^c = (x_i - 1 + \mu)\hat{\mathbf{x}} + y_i\hat{\mathbf{y}} + z_i\hat{\mathbf{z}} \tag{24}$$

then the initial guess for the control strategy is

$$\hat{\mathbf{u}}_i^0 = \frac{\mathbf{r}_i^c}{\left\|\mathbf{r}_i^c\right\|} \tag{25}$$

By definition, $\hat{\mathbf{u}}_i^0$ possesses unit magnitude.

Satisfying the equations of motion for a guessed trajectory: "EOM-NR" A third initial control strategy involves the definition of the control vector at each epoch, $\mathbf{u}_i$, by satisfying the equations of motion for either a circular or static-point-type initial guess for the path, that is,

$$f(\mathbf{u}_i^0) = \tilde{\mathbf{a}}_i + 2\left({}^I\omega^R \times \tilde{\mathbf{v}}_i\right) + \nabla U(\mathbf{r}_i) - \beta(\hat{\ell}(t_i)\cdot\mathbf{u}_i^0)^2\mathbf{u}_i^0 = \mathbf{0} \tag{26}$$

where $\tilde{\mathbf{a}}_i$ and $\tilde{\mathbf{v}}_i$ indicate a central difference approximation for the acceleration and velocity, respectively, based on the initial guess for the path (a circle or a point). A Newton-Raphson iteration scheme is used to solve this nonlinear equation, with each $\mathbf{u}_i^0$ initially directed away from the Moon. The converged control history then serves as the input control history, $\mathbf{u}^0$, to the numerical algorithms. Unlike the other strategies, the control vector is not initially a magnitude of one, and the numerical solution process (e.g., finite-difference method) is expected to render a viable trajectory and a control profile where each $\hat{\mathbf{u}}_i$ is unit length. This strategy is labeled "EOM-NR" in Table **1**.

Required acceleration: "RAA" A fourth, simpler initial control strategy assumes that the initial guess trajectory is already a solution to the equations of motion, Eq. (1), with the caveat that the sail provides any additional, required applied acceleration without regard to feasibility or practicality (i.e., the sail is assumed capable of unlimited, variable thrust, independent of direction). Therefore, if the applied acceleration that is required to solve the equations of motion appears as

$$\mathbf{a}_{raa,i} = \tilde{\mathbf{a}}_i + 2\left({}^I\omega^R \times \tilde{\mathbf{v}}_i\right) + \nabla U(\mathbf{r}_i) \tag{27}$$

where $\tilde{\mathbf{a}}_i$ and $\tilde{\mathbf{v}}_i$ indicate a central difference approximation based on the initial guess for the path (a circle or a point) of the acceleration and velocity, respectively, then the initial guess for the control strategy is

$$\hat{\mathbf{u}}_i^0 = \frac{\mathbf{a}_{raa,i}}{\left\|\mathbf{a}_{raa,i}\right\|} \tag{28}$$

This strategy is labeled "RAA" for "required applied acceleration" in Table **1**.

Parallel to the pseudo-gravity gradient: "∇U" The fifth option in delivering the initial guess for the control

history (labeled "∇U" in Table **1**) is similar in concept to the RAA as presented in Eqs. (27) and (28), except that only the pseudo-gravity gradient, $\nabla U(r)$, is involved, that is,

$$\hat{\mathbf{u}}_i^0 = \frac{\nabla U(\mathbf{r})}{\|\nabla U(\mathbf{r})\|} \tag{29}$$

Of course, if the sailcraft moves relative to the rotating frame, for example, when the trajectory is a circle, the relative and the Coriolis acceleration terms are non-zero. Therefore, this initial guess may be more appropriate in combination with a static point initial guess for the path. The pseudo-gravity gradient for the control direction is a critical quantity to develop equilibrium surfaces in the problem and may yield some insight (e.g., McInnes [16]).

Along the sunline: "$\hat{\ell}$" The final initial guess concept for the control history is simple and completely independent of the initial guess associated with the trajectory. To seed the corrections process, the control strategy assumes that the sail-face normal is parallel to the sunlight direction (labeled "$\hat{\ell}$" in Table **1**).

For all initial guess combinations, the directions of the sail-face normal at the nodes along the trajectory, as well as the path itself, align to solve the equations of motion *via* a numerical boundary value problem solver. For this analysis, the augmented finite differences presented by Wawrzyniak and Howell are employed [21]. Note that the number of nodes, n, also affects whether or not a solutions converges. Throughout this analysis, $n = 101$.

4.1.3. Characteristic Acceleration

For an ideal sail, the characteristic acceleration, β (nondimensional) or a_0 (mm/s^2), is the parameter that encapsulates the sailcraft area, mass, and reflective properties. For a perfectly reflecting solar sail, the characteristic acceleration is

$$a_0 = \eta \frac{2P}{\sigma_s + m_p / A} \tag{30}$$

where P is the nominal solar radiation pressure at 1 AU (4.56e-6 N/m^2), m_p is the mass of the payload and spacecraft excluding the sail and associated support structure, and A is the area of the sail. The $2P$ in the numerator assumes a perfect specular reflection, and, thus, momentum transfer from the photons, on a flat sail. An efficiency factor, η, represents absorption and non-perfect reflection and is typically 0.85-0.90 [16]. The sail-loading parameter, σ (also known as areal density), is simply a mass to area ratio corresponding to the sail and associated structure and is the primary metric for hardware performance.

A recent sailcraft design for NASA's Space Technology competition (ST9) was built by L'Garde with overall characteristic acceleration, a_0, of 0.58 mm/s^2, while the characteristic acceleration of the sail and its support structure alone is closer to 1.70 mm/s^2 (0.212 to 0.623 in units of nondimensional acceleration, respectively) [28]. The study in ref. [9] assumes that the ST9 sailcraft can be scaled so that the overall characteristic acceleration is 1.2 mm/s^2. The IKAROS spacecraft, the first mission to successfully demonstrate the deployment of a sail in space, has a characteristic acceleration of 0.364e-3 mm/s^2 [29]. NASA recently launched and deployed the NanoSail-D2, which possesses a characteristic acceleration of 0.02 mm/s^2 [30]. The Planetary Society's *LightSail-1*, which is comprised of three cubesats, is expected to deliver a characteristic acceleration of 0.057 mm/s^2 [31]. These sails (and others) are designed to demonstrate the deployment of a sail in space and measure the effect of solar radiation pressure on a sail. Future solar sail flight projects may be designed to maximize the characteristic acceleration. This investigation surveys a range of characteristic accelerations to evaluate the level of technology to support a sailcraft mission that addresses the LSP coverage problem.

4.2. Critical Metrics

A trajectory designer typically constructs an orbit while considering various trade-offs. Formulating the design strategy as a single-objective optimization problem is not generally appropriate, as many variables can constitute the "cost." In extending the formulation to a multi-objective optimization problem, suitable solutions may be overlooked and poor knowledge of the solution space impedes progress. In essence, the design goals typically involve optimizing "operability" while meeting mission constraints.

In designing an orbit to satisfy the requirements for a specific mission scenario, path constraints such as minimum elevation angle and maximum altitude are incorporated, i.e., Eqs. (8) and (9), into the trajectory design. However, for a given spacecraft configuration, the elevation angle might be maximized for more margin in a visibility requirement, or, if the vehicle's motion is contained below one of the Lagrange points, to reduce the range of azimuth angles, perhaps allowing a fixed antenna at the south pole. Alternatively, a lower maximum altitude also can reduce the required antenna power.

Trajectory considerations must also be balanced with the design of the sailcraft itself. Orbits associated with lower characteristic accelerations are more feasible with near-future technology; however, fewer trajectory options are available. Orbits for an ideal sail that are associated with high pitch angles (α) along the trajectory may be infeasible when the forces on the sail are modeled with higher fidelity (e.g., optical force model), as previously noted. Finally, solutions that require smaller torques to orient the sailcraft to the required attitude may be easier to maintain. The objective in designing a solar sail spacecraft is to minimize mass while maximizing area. Incorporating an attitude control system adds mass, thus, this final metric of "turnability," along with characteristic acceleration, is of great interest.

4.2.1. Specific Transverse Torque, or "Turnability"

Some recently published results for solar sail attitude control are relevant. Sailcraft, like other space vehicles, can be spin stabilized, three axis stabilized, or stabilized by a

gravity gradient, among other methods. Of the sailcraft that are spin stabilized, the attitude can be modified by thrusters [32,33] or by translating and tilting the sail panels [32], or by reflectivity control devices that adjust the sail optical properties [34]. Three axis stabilized sailcraft may be re-oriented *via* (1) reaction wheels [35,36], or control vanes [35], (2) purposefully offsetting the center of mass and the center of pressure that yields a torque *via* a movable boom [37] or translating mass [38,39], (3) small thrusters at the tips of the sail masts [38], (4) magnetic torquers, or (5) a combination of two or more of these devices [40]. Other sail concepts are stabilized *via* gravity gradients and magnetic torquers [41,42].

If the sail is modeled as a rigid body, and the body axes are aligned with the principal moments of inertia, Euler's familiar equations of motion govern the relationship between the applied torques, the body rates, and the angular acceleration, that is,

$$\mathbf{M} = \mathbf{I} \cdot {}^{I}\dot{\omega}^{B} + {}^{I}\omega^{B} \times \mathbf{I} \cdot {}^{I}\omega^{B} \tag{31}$$

where $\mathbf{I}$ is the central, principal inertia dyadic, ${}^{I}\omega^{B}$ is the angular velocity of the body-fixed frame with respect to the inertial frame, and $\mathbf{M}$ is the vector of external torques required to control the spacecraft attitude. The derivation of ${}^{I}\omega^{B}$ as well as ${}^{I}\dot{\omega}^{B}$ as functions of Eulerian rotations appear in Section 2.3. Solar sails are generally designed to be symmetric about one principal axis of inertia, such that an axial moment of inertia, I_a, is approximately twice that of the transverse moment of inertia, I_t. If the x axis in the body frame is the axis of symmetry and the spacecraft spins about that axis at a constant rate, ω_{x0}, then Eq. (31), reduces to the following scalar equations

$$\begin{aligned} M_x &= 2I_t \cancel{\dot{\omega}_{x0}} \to 0 \\ M_y &= I_t(\dot{\omega}_y - \omega_z \omega_{x0}) \\ M_z &= I_t(\dot{\omega}_z + \omega_{x0}\omega_y) \end{aligned} \tag{32}$$

where ω_{x0}, ω_y, and ω_z are the components of ${}^{I}\omega^{B}$ in a body-fixed frame. If the sailcraft is three axis stabilized (i.e., not spinning and $\omega_{x0} = 0$), Eqs. (32) further reduce to

$$\begin{aligned} M_x &= 0 \\ M_y &= I_t\dot{\omega}_y \\ M_z &= I_t\dot{\omega}_z \end{aligned} \tag{33}$$

It is clear from both the spinning (Eq. (32)) and the three axis stabilized (Eq. (33)) types of motion that the ability to successfully complete attitude turns is limited by the available torques in the pitch and yaw directions ($\hat{\mathbf{y}}^{iv}$ and $\hat{\mathbf{z}}^{iv}$ axes, respectively).

Two recent studies lend insight into the relationship between the capabilities of a three axis stabilized sailcraft and the associated maximum angular accelerations. Citing key driving performance requirements from three previous NASA mission studies where the control mechanism is a movable boom and the spacecraft is three axis stabilized, Price *et al.* [37] establishes an upper limit for pitch and yaw accelerations of 2.3e-9 deg/s^2. More recently, Wie [35] establishes maximum pitch and yaw accelerations of 28.1e-6 deg/s^2 and a maximum turn rate of 0.02 deg/s when the control mechanism for a three axis stabilized sailcraft is sail panel translation and rotation. The parameters for a 40-by-40 meter sail design that Wie uses originate from a mix of ST6 and ST7 designs [35]: the sail moments of inertia are $I_x = 6000\ \text{kg}\cdot\text{m}^2$ and $I_y, I_z = 3000\ \text{kg}\cdot\text{m}^2$ with an areal density of 0.111 kg/m^2 and a characteristic acceleration of 0.0737 mm/s^2. The maximum roll-control torque for the ST6/7 sailcraft of ±1.34e-3 N·m and the maximum pitch- and yaw-control torques are ±1.45e-3 N·m; the corresponding maximum angular accelerations are ±13.0e-6 deg/s^2 and ±28.1e-6 deg/s^2, respectively.

When the spacecraft is spin stabilized such that ω_x is constant, i.e., $\omega_x = \omega_{x0}$, the cross terms in Eq. (32) must be considered. In a three axis stabilized case, Eq. (33), the available torque in a particular direction is employed to rotate the spacecraft about that direction. When a spacecraft is spin stabilized about the x axis, the same turn requires additional torque about the y and z axes. A configuration similar to the three axis spacecraft is employed by Wie for the analysis of a sailcraft spinning at 5 rotations per hour [32]. The IKAROS sailcraft employs liquid crystal displays to change the reflective properties of the sail material for turning; however, its primary attitude control system is a set of thrusters on the central bus [29].

If the required rotational rates and accelerations associated with a particular trajectory are known, a specific torque about each axis can be determined. Because the labeling of the transverse y and z axes is arbitrary, the concept of a specific transverse torque is convenient. This metric characterizes the vehicle's ability to turn and is calculated from the transverse torques in either Eq. (32) or Eq. (33), that is,

$$\mathscr{M}_t = \sqrt{\left(\frac{M_y}{I_t}\right)^2 + \left(\frac{M_z}{I_t}\right)^2} \tag{34}$$

For a given trajectory and nominal control profile, different specific transverse torques are required that depend on the spin rate. The maximum specific transverse torques corresponding to a three axis stabilized sailcraft (non-spinning), $\mathscr{M}_{t,3AS}$, and one spinning at 5 rotations per hour, $\mathscr{M}_{t,spin}$, are examined.

4.2.2. Summary of Critical Metrics for "Operability"

This investigation is focused on six critical metrics for assessing different sailcraft trajectories and the associated control profiles. In summary, these metrics are

- Sail characteristic acceleration, a_0

- Maximum specific transverse torque at any time along the orbit, $\mathcal{M}_t$
- Largest pitch angle at any time along the orbit, α
- Lowest elevation angle at any time along the orbit, E
- Highest altitude at any time along the orbit, A
- Largest range of azimuth angles throughout the orbit

While the items in this list may be incorporated in a multi-variable optimization scheme as either parameters to optimize or as constraints, the goal of this investigation is an improved understanding of the solution space, motivating a survey. The insight gained from this survey is necessary to initialize a process that optimizes one or more of these critical metrics. Finally, additional critical metrics may be identified, or some current metrics may be disregarded at some future time. A new search would then be conducted using these same techniques.

5. RESULTS

The primary purpose of using a simple, lower-fidelity, augmented finite difference method to propagate states and compute solutions is to quickly and easily examine the design space for a solar-sail spacecraft in orbit near the Moon. Using the MATLAB numerical computing environment, over 10 million combinations of initial guesses are used to generate trajectories for the survey. The computation employed up to eight cores on five platforms and took approximately one week. Different combinations of initial guess strategies lead to different solutions. This is especially true when comparing trajectories that arise from circular initial guesses for the path to those that arise from initial guesses that collapse the trajectory to a single point. A general survey of the solution space for all combinations of initial guesses is a first step in understanding the design space. A viable solution generated from any method possesses characteristics that can be employed to select any particular orbit for further study.

5.1. Survey of Initial Guess Combinations

The survey is developed to incorporate two versions of a finite-difference approximation [21], three strategies to produce an initial guess for the path, six strategies to deliver an initial control profile, and the investigation also includes an examination of various elevation-angle constraints. The three path strategies include a retrograde circular orbit, a point hovering in the xz plane, and a prograde circular orbit. The circular trajectories all possess periods equal to the solar synodic period. Of the initial control profiles, the α^* and $\hat{\ell}$ approaches are most successful in generating solutions for any type of initial path. The EOM-NR and Moon control approaches only result in converged solutions when the initial guess for the path is a circular retrograde orbit. The ∇U and the RAA approaches are successful when the initial guess for the path is a prograde or a retrograde circle, but not when the initial guess is a point.

Any one initial control strategy is not necessarily superior to any other, however, the α^* and $\hat{\ell}$ strategies converged more often than the other types of initial guesses for the control profile. An appropriate plan for examining the design space is the selection of a range of characteristic accelerations and path constraints and, then, the generation of solutions based on multiple combinations of initial guesses for the path and control.

5.2. Spacecraft-Driven Critical Metrics

Critical metrics generally emerge as one of two types: those that drive the spacecraft design and those that drive the ground station design. To fly a particular path, the vehicle must possess a specific characteristic acceleration, a_0, be able to change its orientation as necessary, and produce thrust at sufficiently high pitch angles. Highlighted below are solutions from the survey that require the smallest a_0, smallest specific transverse torques, and smallest maximum pitch angles in their respective categories.

5.2.1. Minimum a_0 to Achieve Various Elevation-Angle Constraints

This analysis is formulated in a CR3B model. In actuality, the obliquity of the lunar orbit with respect to the Earth is 6.688° and the Moon's orbit is a secularly precessing ellipse with respect to an inertial frame. Additional margin to accommodate lunar surface features and incorporate a more realistic ephemeris model is added to the obliquity to determine $E_{\min}$. For the broader survey of the design space to support a lunar communications relay, an elevation-angle constraint of $E_{\min} = 15^\circ$ and altitude constraint of $A_{\max}$ = 384,400 km is assumed (see Fig. **2** for an illustration of $E_{\min}$ and $A_{\max}$). For these constraints, the smallest sail characteristic acceleration examined in this survey that satisfies these constraints is $a_0 = 1.3$ mm/s^2. Smaller values of a_0 examined in this survey (i.e., 1.25 mm/s^2) are insufficient to push the vehicle sufficiently far below the Moon to satisfy the elevation-angle constraint.

In the present survey, when the elevation-angle constraint is relaxed, solutions emerge for sails with smaller characteristic accelerations. Moon-centered offset orbits conforming to the lower constraints might not be viewable at all times from an outpost near the lunar south pole. Orbits offset below L_1 and L_2 may be useful as relays for a base near lower lunar latitudes, but on the near or far side of the Moon, respectively, and may require lower elevation-angle constraints. The lowest overall characteristic accelerations for a spacecraft equipped with a solar sail considered in this survey that meet these elevation-angle constraints under the three locations are listed in Table **2**.

Since a discrete set of characteristic accelerations is considered, the actual minimum value of a_0 that conforms may be slightly less than the values in this table. The data in the table indicate that sails with higher characteristic accelerations are required for orbits below the Earth-Moon L_1 point or the Moon for a given elevation-angle constraint; relatively lower characteristic accelerations are viable for sail

(**a**) Top view, *xy*

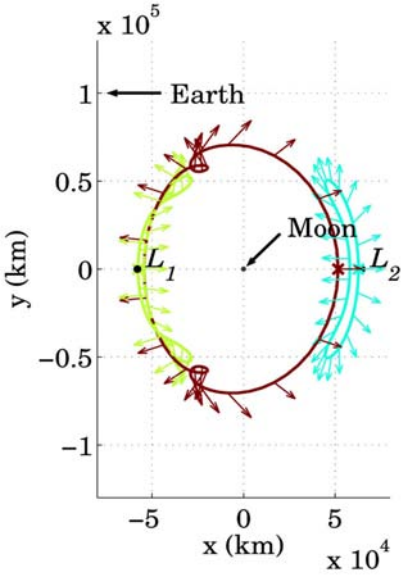

(**b**) Side view, *xz*

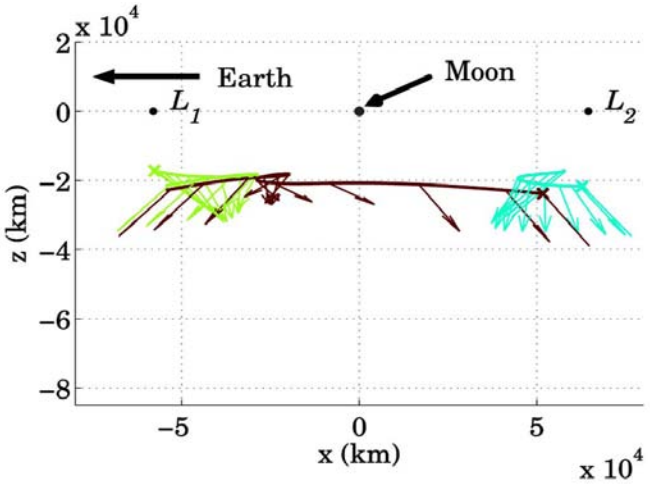

Fig. (11). Orbits below L_1, the Moon, and L_2 that conform to the 15° elevation-angle constraint and possess the smallest possible a_0.

trajectories below the L_2 point. Certainly, a_0 could be minimized using an optimization scheme, and this broad survey simply offers a sense of the solutions available. The results from this survey yield a starting point for an optimization scheme based solely on characteristic acceleration or in combination with other metrics of interest.

Table 2. Smallest a_0 (mm/s^2) Required for Orbits Located Below the Moon and the Earth-Moon L_1 and L_2 Points Based on Elevation Angle

E_{min}:	4°	6°	9°	12 °	15°
L_1	0.58	1.00	1.25	1.50	1.60
Moon	0.55	0.75	1.00	1.50	1.60
L_2	0.40	0.55	1.00	1.25	1.30

A variety of solutions exist for sails with the lowest value of characteristic acceleration that is required for the three locations. One such orbit appears for each location in Fig. (**11**). As before, the Sun is defined to move clockwise about the Moon as viewed in Fig. (**10**), originating at a position along the $-x$ axis. The maroon and turquoise paths originate opposite to the Sun, while the lime-green path originates on the Sun-side with respect to its center. Initial motion along all three paths proceeds in the $-y$ direction as the Sun moves in the $+y$ direction. In fact, the Sun moves in a clockwise, retrograde, fashion one half-period out of phase with a spacecraft moving along the retrograde maroon and turquoise paths. Motion along the lime-green path, however, is prograde, as a spacecraft along that path moves in a counter-clockwise fashion. Because of the motion of the Sun, prograde orbits originate on the left side of the orbit and motion is counter-clockwise while retrograde orbits orbits originate on the right side and motion is clockwise as projected on the *xy* plane. Recall that the duration of each orbit is one sidereal month (29.5 days).

For a given value of a_0, an abundance of solutions exist. From a set of solutions with the lowest a_0, the trajectories appearing in Fig. (**11**) are selected based on the smallest maximum specific transverse torque ($\mathcal{M}_{t,spin}$) along the orbit for a spinning sailcraft.[2] Critical metrics, such as the maximum $\mathcal{M}_{t,3AS}$ if the sailcraft is three axis stabilized (3AS), the maximum pitch angle (α), and the minimum elevation angle (E), along these three trajectories appear in Table **3**. Pitch angles associated with the orbits in Fig. (**11**) are all less than 55°, indicating that the solutions may successfully transition to a higher-fidelity sailcraft SRP model.

As the value of the sailcraft characteristic acceleration is increased, more trajectory solutions are available. By fixing $a_0 = 1.70$ mm/s^2, a comparison with other critical metrics is possible. A sail characteristic acceleration this large is not possible with current technology. However, based on the results in Table **2**, a sail must possess a characteristic acceleration near this magnitude to satisfy mission constraints (e.g., $E \geq 15^\circ$ under L_1, L_2, and the Moon), and a requirement for future sail hardware technology is now established. For the rest of this investigation, to compare the broadest set of metrics, $a_0 = 1.70$ mm/s^2. Note that the techniques employed to conduct this survey are applicable to missions with different path constraints and sailcraft with different physical characteristics.

[2]If the smallest maximum $\mathcal{M}_{t,3AS}$ along the orbit for a three axis stabilized sailcraft is used as the selection criteria, similar solutions appear under the Lagrange points and the same solution appears below the Moon.

Table 3. Critical Metrics for Orbits Conforming to $E \geq 15°$, Selected by a_0 and $\mathcal{M}_{t,spin}$

	a_0	Max $\mathcal{M}_{t,spin}$	Max $\mathcal{M}_{t,3AS}$	Max α	Min E
L_1	1.60 mm/s^2	1.21e-6 deg/s^2	2.26e-9 deg/s^2	43.99°	15.00°
Moon	1.60 mm/s^2	4.39e-6 deg/s^2	11.91e-9 deg/s^2	48.66°	15.00°
L_2	1.30 mm/s^2	0.78e-6 deg/s^2	1.33e-9 deg/s^2	51.91°	15.00°

(**a**) Top view, *xy* (**b**) Side view, *xz*

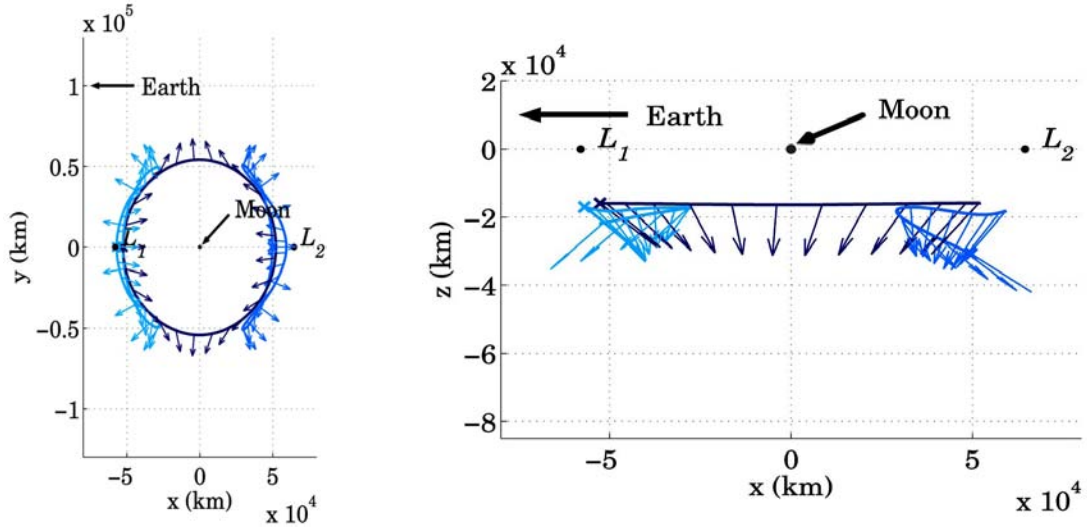

Fig. (12). Orbits under L_1, the Moon, and L_2 that possess the smallest possible $M_{t,spin}$ for $a_0 = 1.70$ mm/s^2.

5.2.2. Specific Transverse Torques

Sample orbits with the smallest maximum $\mathcal{M}_{t,spin}$ for a spin stabilized spacecraft corresponding to a sail characteristic acceleration of $a_0 = 1.70$ mm/s^2 appear in Fig. (**12**). For the dark-blue path below the Moon in Fig. (**12**), the trajectory originates on the $-x$ side of the Moon and the spacecraft moves in a counter-clockwise, prograde, fashion. Note that the arrows that represent the direction of the sail-face normal for the portions of the path near the x axis appear to be directed "inward" as viewed from above the xy plane (Fig. **12**) for a prograde orbit and "outward" for a retrograde orbit; the sail-face normal is constrained to be directed away from the Sun, which moves clockwise about the system. Consequently, the sunlight direction is generally aligned with the projection of the sail-face normal vector when the normal vector is projected into the xy plane. Both paths corresponding to the smallest $\mathcal{M}_{t,spin}$ below the Lagrange points in Fig. **12** are considered prograde orbits as well.

Critical metrics for the orbits with the smallest maximum $\mathcal{M}_{t,spin}$ are listed in Table **4**. Recall that $\mathcal{M}_{t,spin}$ and $\mathcal{M}_{t,3AS}$ are independently determined after the orbit is generated and is based on the angles α and δ, as well as the spin rate of the vehicle. The equation for the body rates appears in the Section 2.3. The maximum $\mathcal{M}_{t,spin}$ for a spin-stabilized and the maximum value for a three axis stabilized spacecraft configuration do not necessarily occur at the same locations along the orbit, as is apparent in Fig. (**13**). Furthermore, the orbit with the smallest maximum $\mathcal{M}_{t,spin}$ is not necessarily the solution with the smallest maximum $\mathcal{M}_{t,3AS}$ from the survey. However, the set of solutions below L_1, the Moon, and L_2 that correspond to the smallest maximum $\mathcal{M}_{t,3AS}$ also resemble the orbits that correspond to the smallest maximum $\mathcal{M}_{t,spin}$ from the survey. Associated critical metrics when the selection criteria is based on the smallest maximum $\mathcal{M}_{t,3AS}$ are listed in Table **5**. The results from the

Table 4. Critical Metrics for Orbits Selected by Smallest Maximum $\mathcal{M}_{t,spin}$

	a_0	Max $\mathcal{M}_{t,spin}$	Max $\mathcal{M}_{t,3AS}$	Max α	Min E
L_1	1.70 mm/s^2	5.74e-7 deg/s^2	5.46e-10 deg/s^2	48.56°	15.01°
Moon	1.70 mm/s^2	2.35e-7 deg/s^2	1.32e-10 deg/s^2	49.42°	15.07°
L_2	1.70 mm/s^2	4.86e-7 deg/s^2	5.71e-10 deg/s^2	54.71°	15.30°

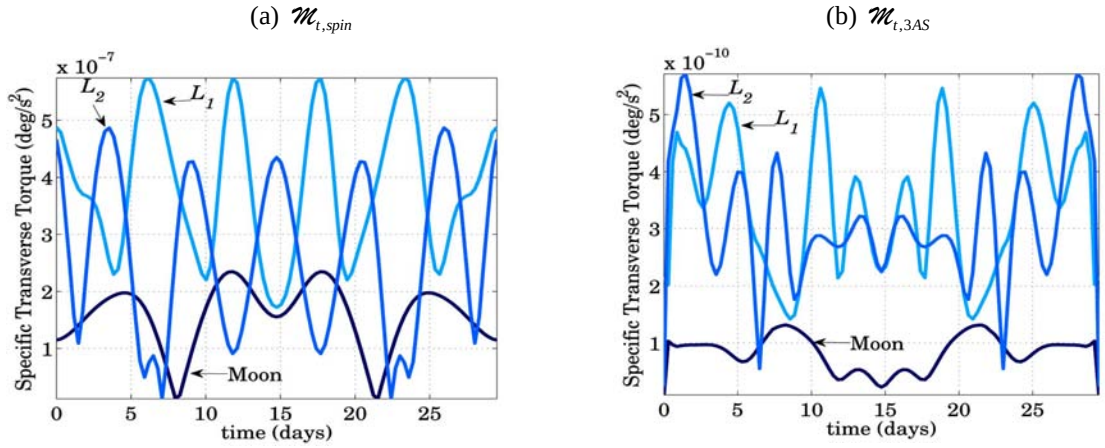

Fig. (13). Specific transverse torque profiles corresponding to orbits in Fig. (**12**), selected by smallest maximum $\mathcal{M}_{t,spin}$.

survey indicate that the trajectories below L_2 that are associated with the smallest specific transverse torques ($\mathcal{M}_{t,spin}$ and $\mathcal{M}_{t,3AS}$) correspond to a maximum pitch angle along the path with a value greater than 55°. The results listed in Tables **4** and **5**, as well as the corresponding paths appearing in Fig. (**12**) and specific transverse torques in Fig. (**13**), correspond to the set of solutions where the maximum pitch angle is restricted to 55°.

5.2.3. Pitch Angle

As discussed previously, depending on the realistic optical and shape properties of a solar sail, the assumption of a perfectly reflecting, flat, ideal sail diverges from a realistic solar sail model for pitch angles greater than 50° to 60°. Furthermore, sail effectiveness is severely attenuated at high pitch angles [16,18]. Therefore, it is desirable to examine trajectories below L_1 and the Moon, as well as L_2 that are associated with the lowest required pitch angles. The three solutions from the survey associated with the lowest required pitch angles for sails with $a_0 = 1.70$ mm/s^2 appear in Fig. (**14**). The associated pitch angle histories for these three trajectories appear in Fig. (**15**). The corresponding critical metrics for these three paths are listed in Table **6**.

5.3. Ground-Based Critical Metrics

If the range of motion or field of view associated with a radio antenna located at the lunar south pole (LSP) is limited, sail trajectories exist that may accommodate this constraint. As mentioned, an elevation-angle constraint of 15° is established in the survey. However, solutions for a sailcraft with a characteristic acceleration value of $a_0 = 1.70$ mm/s^2 exist that do not activate this constraint. It is also useful to identify the range of altitudes necessary for the orbits associated with a particular sailcraft characteristic acceleration. Finally, the design of any facility at the LSP benefits from information on the field of view. These ground-based critical metrics are examined for a sailcraft with $a_0 = 1.70$ mm/s^2.

5.3.1. Elevation Angle

The first critical metric for ground-station design is the elevation angle. While a constraint of 15° is imposed in this survey, any solutions not activated by this constraint lend insight into other available options. The three sample orbits below L_1, the Moon, and L_2 that appear in Fig. (**16**) possess the associated critical metrics as listed in Table **7**.

Unfortunately, little extra margin is available for orbits under L_1 and the Moon. However, solutions do exist below L_2 that possess a minimum elevation angle along the path of nearly 18°.[3] The relationship between a_0 and E is understandable within the context of a trade-off between a_0 and E, that is, a lower a_0 is required for trajectories under L_2, as demonstrated in Section 5.2.1. Alternatively, a greater minimum elevation angle is available under L_2 as compared to L_1, or even the Moon, for the same a_0.

5.3.2. Altitude

The distance of a vehicle from a station on the ground drives the power requirements for the transmitting and receiving antennas both at the ground and on the spacecraft. Therefore, it is useful to assess the range of distances from the lunar south pole for a family of solutions when designing a mission and communications system. The altitude of the spacecraft in orbit below the Moon depends upon the dynamics of the system, which is based on the gravity of the primaries and the characteristic acceleration, a_0, of the sail. Sailcraft with larger values of a_0 may orbit either closer to the Moon or at higher elevation angles. For a characteristic acceleration of 1.70 mm/s^2, the smallest maximum altitude along any trajectory from the survey is 55009 km, while the largest maximum altitude is 141310 km. These two paths, both below the Moon, are plotted in Fig. (**17**), and their

[3]The path under L_2 is selected in post-processing and originates from the set of solutions with $\alpha \in [0,55^\circ]$. Orbits with larger minimum elevation angles exist that require larger maximum pitch angles along the path.

Table 5. Critical Metrics for Orbits Selected by Smallest Maximum $\mathcal{M}_{t,3AS}$

	a_0	Max $\mathcal{M}_{t,spin}$	Max $\mathcal{M}_{t,3AS}$	Max α	Min E
L_1	1.70 mm/s^2	6.25e-7 deg/s^2	3.43e-10 deg/s^2	46.44°	15.41°
Moon	1.70 mm/s^2	2.35e-7 deg/s^2	1.29e-10 deg/s^2	49.36°	15.07°
L_2	1.70 mm/s^2	5.58e-7 deg/s^2	3.77e-10 deg/s^2	53.82°	15.78°

(**a**) Top view, *xy* (**b**) Side view, *xz*

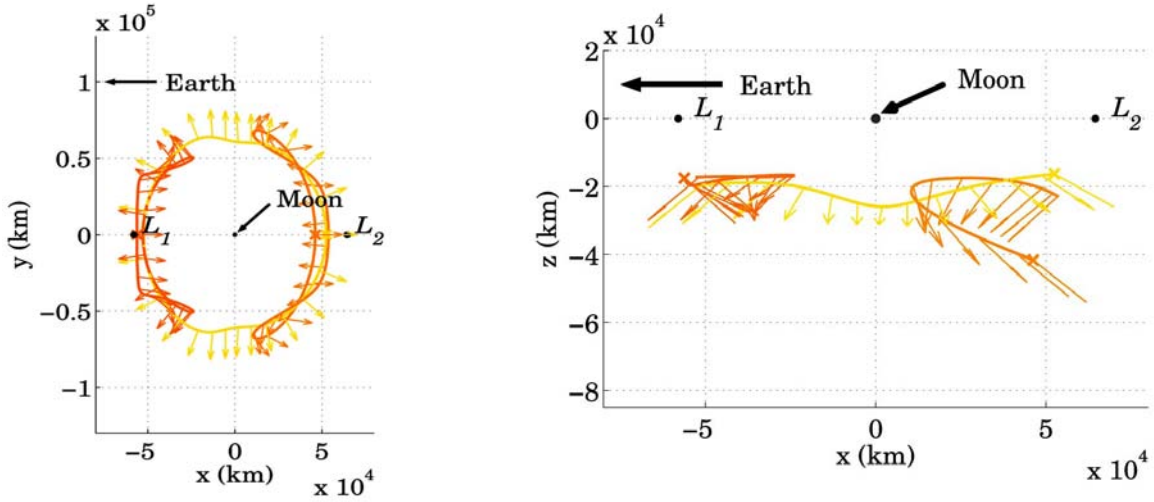

Fig. (14). Sample orbits offset below L_1, the Moon, and L_2 that conform to the 15° elevation-angle constraint and possess the smallest required pitch angles at any point along the trajectory.

critical metrics are listed in Table **8**. The red path originates below L_2 and is a retrograde orbit, while the aqua path originates below L_1 and is a prograde orbit. Note that the red path in Fig. (**17**) is selected from a set of solutions where the maximum pitch angle at any point along the trajectory is less than 55°.

5.3.3. Azimuth Angle Ranges

For simplicity, assume that the antenna is fixed on the lunar surface and is always directed toward the sailcraft relay. If the sailcraft is located below L_1, the smallest swath width required of ground antenna is 64.4°. The smallest swath width associated with a sail below L_2 is 70.2°. The two trajectories associated with these swath widths appear in Fig. (**18**), and their respective critical metrics are listed in Table **9**.

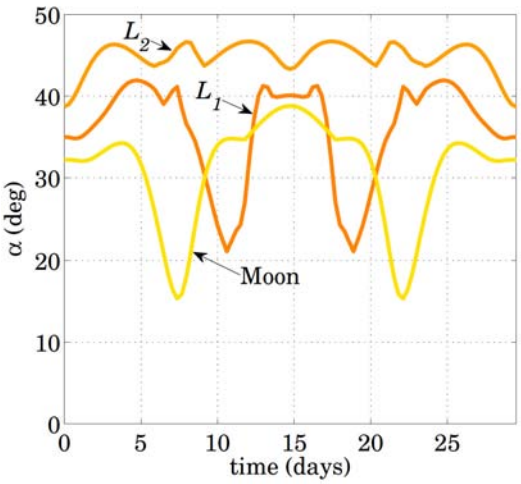

Fig. (15). Pitch angle histories for orbits in Fig. (**14**).

Table 6. Critical Metrics for Orbits Selected by Smallest Required Pitch Angle, α

	a_0	Max $\mathcal{M}_{t,spin}$	Max $\mathcal{M}_{t,3AS}$	Max α	Min E
L_1	1.70 mm/s^2	2.09e-6 deg/s^2	5.86e-9 deg/s^2	41.95°	15.00°
Moon	1.70 mm/s^2	1.59e-6 deg/s^2	1.28e-9 deg/s^2	38.83°	15.00°
L_2	1.70 mm/s^2	1.93e-6 deg/s^2	1.53e-9 deg/s^2	46.71°	15.00°

6. DISCUSSION

Some general observations are notable, based on the results from the survey in the Earth-Moon system. First, trajectory options for a spacecraft relay, to support a facility at the lunar south pole, exist for sailcraft with characteristic accelerations of 1.3 mm/s^2 or greater. Although solar sailing has only recently been demonstrated in flight, the recent design of the sailcraft for the ST9 ground demonstration delivers an overall characteristic acceleration of 0.58 mm/s^2 (including payload and attitude control system) while the characteristic acceleration supplied solely by the sail and structure is 1.7 mm/s^2 [28]. However, a solar sail alone is not the only option for a single-vehicle relay to deliver LSP coverage. Other researchers propose hybrid propulsion systems that are based on a combination of a solar sail and low-thrust technologies. While the survey techniques developed for this analysis are applied to solar sails, the formulations are also adaptable for hybrid or other systems where a continual thrust component is available.

Second, if the vehicle is either spin-stabilized or three axis stabilized, the trajectory options resulting from this survey require attitude control authority within the assumptions employed in other investigations of solar sail attitude dynamics and control. The maximum specific transverse torques for a sailcraft spinning at 5 rotations per hour are less than the 28.1e-6 deg/s^2 assumption published by Wie for a three axis stabilized spacecraft [35]. To remain in an orbit offset below the Moon, a sailcraft must continually reorient itself. The control profiles for these sample orbits are essentially continuous, as returned by the numerical BVP solver employed to generate the trajectory. In reality, it may be advantageous to command the spacecraft in a "turn-and-hold" scheme, whereby the orientation is held in an inertially fixed attitude for some length of time (e.g., 2-3 days), and then reoriented to a new attitude [43]. In this scheme, it is presumed that lower specific transverse torques from the continuous case translate to lower specific transverse torques in a turn-and-hold scheme.

Returning to the assumption of a vehicle that continually reorients, it is observed that larger specific torques from the three axis stabilized attitude scheme are apparently correlated with larger specific torques from the spin-stabilized attitude scheme. Statistics from the millions of sample orbits generated in this survey suggest a power

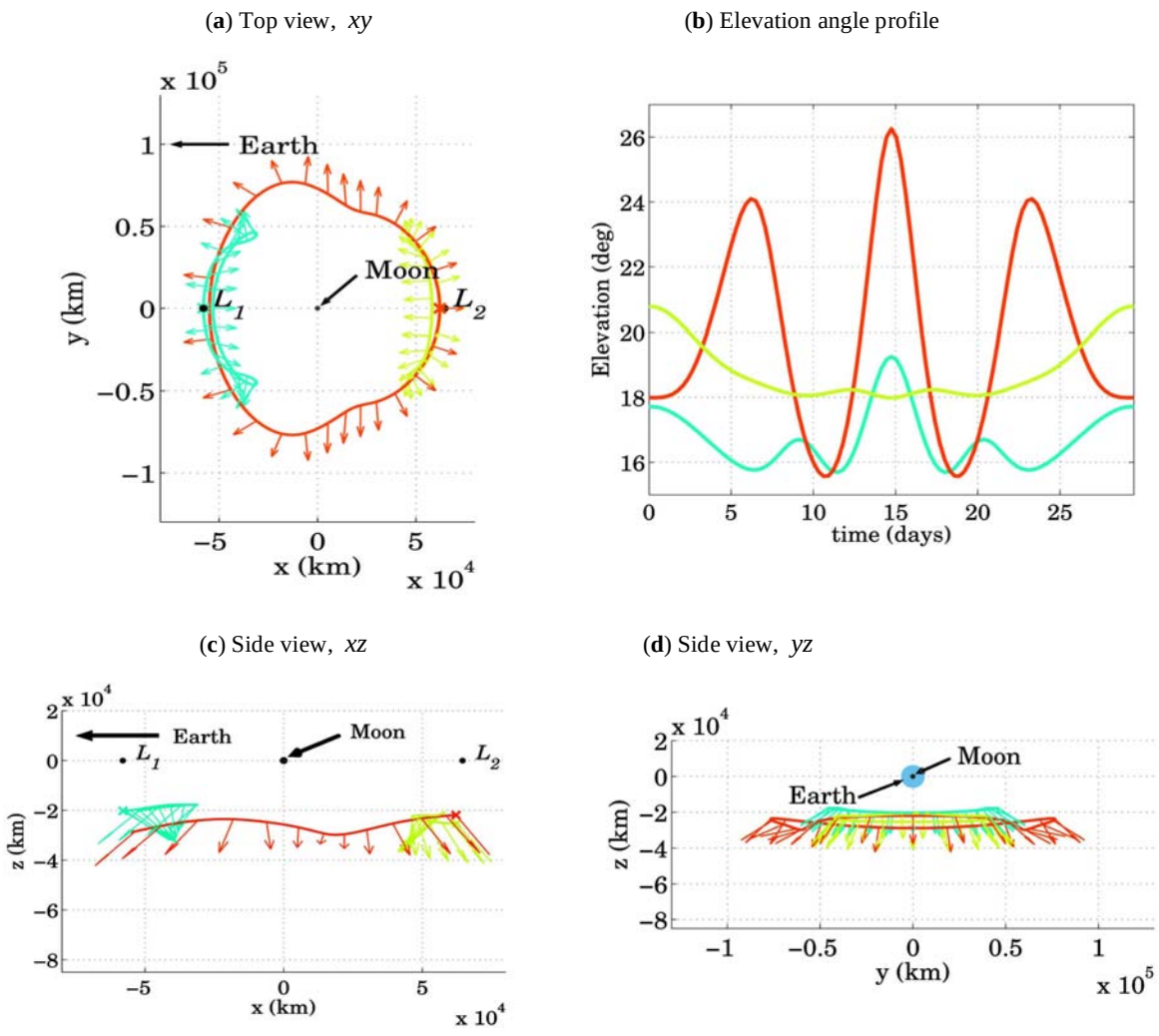

Fig. (16). Orbits under L_1, the Moon, and L_2 possessing the largest minimum elevation angle.

Table 7. Critical Metrics for Orbits Selected by Largest Minimum Elevation Angle, *E*

	a_0	Max $\mathcal{M}_{t,spin}$	Max $\mathcal{M}_{t,3AS}$	Max α	Min E
L_1	1.70 mm/s^2	0.82e-6 deg/s^2	0.88e-9 deg/s^2	46.55°	15.69°
Moon	1.70 mm/s^2	2.45e-6 deg/s^2	2.94e-9 deg/s^2	50.55°	15.57°
L_2	1.70 mm/s^2	1.29e-6 deg/s^2	0.71e-9 deg/s^2	54.62°	17.98°

Table 8. Critical Metrics for Orbits Selected by Altitude

	a_0	Max $\mathcal{M}_{t,spin}$	Max $\mathcal{M}_{t,3AS}$	Max α	Min E	Max A
Farthest	1.70 mm/s^2	4.19e-6 deg/s^2	9.26e-9 deg/s^2	54.97°	15.00°	141310 km
Nearest	1.70 mm/s^2	0.85e-6 deg/s^2	0.75e-9 deg/s^2	50.01°	15.00°	55009 km

relationship between the maximum $\mathcal{M}_{t,spin}$ and $\mathcal{M}_{t,3AS}$, that is,

$$\mathcal{M}_{t,3AS} = (\mathcal{M}_{t,spin})^P \qquad (35)$$

$$P = 1.50 \pm 0.075$$

when $\mathcal{M}_{t,spin}$ and $\mathcal{M}_{t,3AS}$ are measured in deg/s^2 and the error bounds are three-standard deviations.[4]

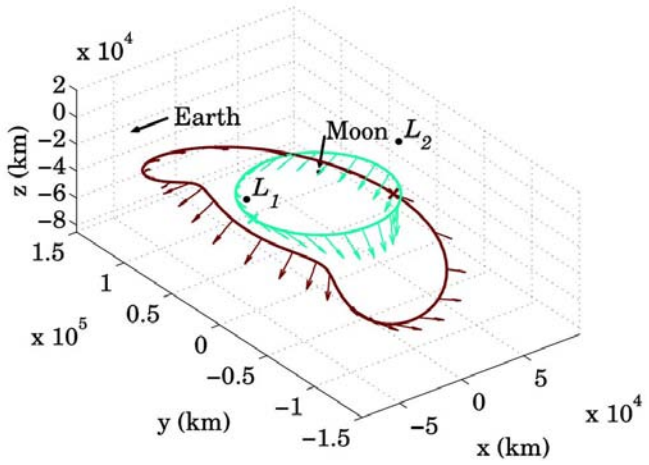

Fig. (17). Orbits possessing the largest and smallest altitudes from a base at the LSP.

Finally, some notable observations about the orbits are summarized. Generally, prograde lunar orbits are"flatter" and evolve at smaller distances relative to the lunar south pole when compared to retrograde lunar orbits. However, retrograde orbits with variable elevation angles may be attractive for some mission-specific considerations. Trajectories below L_2 require smaller sail characteristic accelerations when compared to trajectories located under L_1 and the Moon. As demonstrated in Section 4.1.1, trajectories exist that naturally transfer from a Moon-centered path to a path located below a Lagrange point. Because sail optical properties degrade over time [44], a sailcraft orbiting below the Moon can be shifted to an orbit under L_2 as a_0 decreases. All of the orbits surveyed are unstable because of their dependencies on a solar sail. Furthermore, all trajectories require some form of flight-path control. Controllability of the flight path is not necessarily related to any particular critical metric employed in this analysis and is the subject for future investigation.

7. CONCLUSIONS AND FUTURE WORK

Solar sail spacecraft supply a solution to the lunar south pole coverage problem that requires only one space vehicle. By employing survey techniques, an understanding of the design space emerges. For a minimum elevation-angle constraint of 15°, a characteristic acceleration of 1.6 mm/s^2 is required to maintain trajectories below L_1 and the Moon, and a characteristic acceleration of 1.3 mm/s^2 is required to orbit below L_2. Solutions exist that both (1) require turning torques that are assumed to be possible for future solar sail spacecraft and (2) do not require excessively large pitch angles with respect to the Sun. Furthermore, if a stationary antenna with a fixed field of view is employed at a facility at the lunar south pole, trajectory options that locate the sailcraft within a 70° swath width exist located below the Lagrange points.

Control profiles of the sailcraft attitude is incorporated into the present study. Future efforts to incorporate trajectory control as a critical metric for trajectory selection is warranted. Finally, higher-fidelity models such as ephemeris positions of the primary bodies and optical or parametric models of the sail force model should also be examined.

ACKNOWLEDGEMENTS

Portions of this work were supported by Purdue University and the School of Aeronautics and Astronautics. Additional support from the College of Science is acknowledged.

[4] $P = 1.39 \pm 0.06$ when $\mathcal{M}_{t,spin}$ and $\mathcal{M}_{t,3AS}$ are measured in rad/s^2.

(**a**) 3D view (**b**)Top view, *xy*

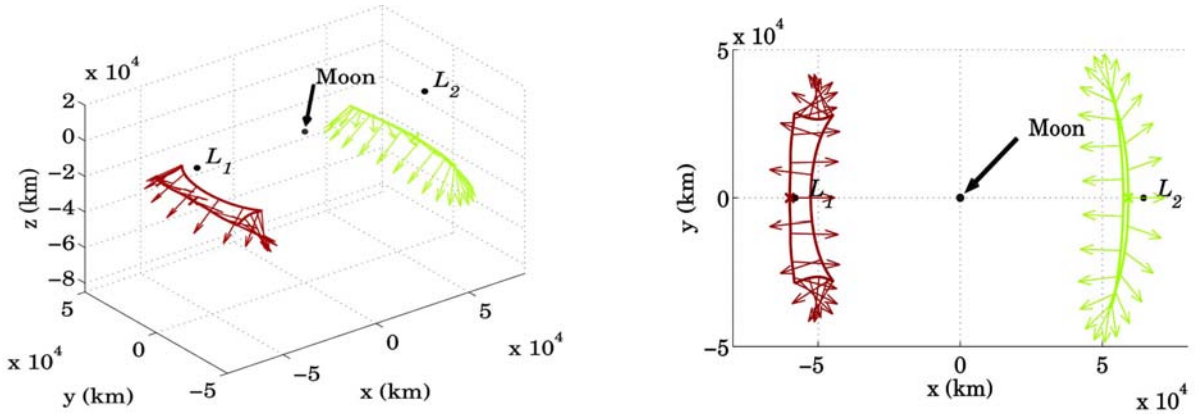

Fig. (18). Orbits under L_1 and L_2 possessing the smallest ranges of azimuth angles.

Table 9. Critical Metrics for Orbits Selected by Azimuth Angle, *Az*, Range

	a_0	Max $\mathcal{M}_{t,spin}$	Max $\mathcal{M}_{t,3AS}$	Max α	Min E	Az Range
L_1	1.70 mm/s^2	3.74e-6 deg/s^2	9.33e-9 deg/s^2	48.77°	15.00°	64.42°
L_2	1.70 mm/s^2	1.24e-6 deg/s^2	0.68e-9 deg/s^2	53.99°	16.60°	70.22°

CONFLICT OF INTEREST

None declared.

REFERENCES

[1] "The Vision for Space Exploration," Tech. Rep. NP-2004-01-334-HQ, National Aeronautics and Space Administration, February 2004.

[2] "NASA Space Communication and Navigation Architecture Recommendations for 2005-2030," Technical Report, Space Communication Architecture Working Group (SCAWG), National Aeronautics and Space Administration, Washington, DC, May 2006.

[3] T. A. Ely, and E. Lieb, "Constellations of elliptical inclined lunar orbits providing polar and global coverage," *Adv. Astronaut. Sci*., vol. 123, pp. 1447-1462, August 2005. Paper No. AAS 05-343.

[4] T. A. Ely, "Stable constellations of frozen elliptical inclined lunar orbits," *J. Astronaut. Sci*., vol. 53, pp. 301-316, July-September 2005.

[5] K. C. Howell, D. J. Grebow, and Z. P. Olikara, "Design using Gauss' perturbing equations with applications to lunar south pole coverage," *Adv. Astronaut. Sci*., vol. 127, pp. 641-670, February 2007. Paper No. AAS 07-143.

[6] D. J. Grebow, M. T. Ozimek, K. C. Howell, and D. C. Folta, "Multibody orbit architectures for lunar south pole coverage," *J. Spacecr. Rocket*., vol. 45, pp. 344-358, March-April 2008.

[7] D. J. Grebow, M. T. Ozimek, and K. C. Howell, "Design of optimal low-thrust lunar pole-sitter missions," *Adv. Astronaut. Sci*., vol. 134, pp. 741-760, February 2009. Paper No. AAS 09-148.

[8] D. J. Grebow, M. T. Ozimek, and K. C. Howell, "Advanced modeling of optimal low-thrust pole-sitter trajectories," *Acta Astronaut*., vol. 67, pp. 991-1001, October-November 2010.

[9] J. L. West, "The lunar polesitter," in AIAA/AAS Astrodynamics Specialist Conference and Exhibit, August 2008. Paper No. AIAA-2008-7073.

[10] M. T. Ozimek, D. J. Grebow, and K. C. Howell, "Design of solar sail trajectories with applications to lunar south pole coverage," *J. Guid. Control, Dyn*., vol. 32, pp. 1884-1897, November-December 2009.

[11] J. Simo and C. McInnes, "Designing displaced lunar orbits using low-thrust propulsion," *J. Guid. Control, Dyn.*, vol. 33, pp. 259-265, January-February 2010.

[12] R. P. Russell, "Global search for planar and three-dimensional periodic orbits near Europa," *J. Astronaut. Sci*., vol. 54, pp. 199-226, April-June 2006.

[13] G. Tsirogiannis, E. Perdios, and V. Markellos, "Improved grid search method: an efficient tool for global computation of periodic orbits," *Celest. Mech. Dyn. Astron*., vol. 103, pp. 49-78, 2009.

[14] D. C. Davis and K. C. Howell, "Trajectory evolution in the multi-body problem with applications in the Saturnian system," in 61st International Astronautical Congress, (Prague, Czech Republic), September 2010. Paper No. IAC-10-C1.1.7.

[15] G. G. Wawrzyniak and K. C. Howell, "Accessing the design space for solar sails in the Earth-Moon system," *Adv. Astronaut. Sci*., vol. 135, pp. 767-786, 2009. Paper No. AAS 09-348.

[16] C. R. McInnes, *Solar Sailing: Technology, Dynamics and Mission Applications*. Space Science and Technology, New York: Springer-Praxis, 1999.

[17] L. Rios-Reyes and D. J. Scheeres, "Solar-sail navigation: Estimation of force, moments, and optical parameters," *J. Guid. Control, Dyn*., vol. 30, pp. 660-668, May-June 2007.

[18] B. Campbell, *An Analysis of Thrust of a Realistic Solar Sail with Focus on a Flight Validation Mission in a Geocentric Orbit.* Washington, DC: Ph.D. Dissertation, The George Washington University, May 2010.

[19] B. Derbes, D. L. Lichodziejewski, and G. Veal, "A 'yank and yaw' control system for solar sails," *Adv. Astronaut. Sci*., vol. 119, pp. 2893-2908, February 2004.

[20] C. R. Ortiz Longo and S. L. Rickman, "Method for the calculation of spacecraft umbra and penumbra shadow terminator points," NASA Technical Paper 3547, Lyndon B. Johnson Space Center, Houston, Texas, April 1995.

[21] G. G. Wawrzyniak and K. C. Howell, "Generating solar sail trajectories in the Earth-Moon system using augmented finite-difference methods," *Int. J. Aerosp. Eng*., vol. 2011, 2011. Article ID 4776197, 13 pages.

[22] D. T. Greenwood, *Principles of Dynamics*. Upper Saddle River, NJ: Prentice Hall, 2 ed., 1988.

[23] S. D. Conte and C. de Boor, *Elementary Numerical Analysis*. New York: McGraw-Hill, 1980.

[24] D. R. Kincaid and E. W. Cheney, *Numerical Analysis: Mathematics of Scientific Computing*. Providence, Rhode Island: American Mathematical Society, 2002.

[25] G. G. Wawrzyniak and K. C. Howell, "Numerical techniques for generating and refining solar sail trajectories," *Adv. Space Res*., (In Press).

[26] T. J. Waters and C. R. McInnes, "Periodic orbits above the ecliptic in the solar-sail restricted three-body problem," *J. Guid. Control, Dyn.*, vol. 30, pp. 687-693, May-June 2007.

[27] M. T. Ozimek, D. J. Grebow, and K. C. Howell, "A collocation approach for computing solar sail lunar pole-sitter orbits," *The Open Aerosp. Eng. J*., vol. 3, pp. 65-75, 2010.

[28] D. Lichodziejewski, B. Derbes, D. Sleight, and T. Mann, "Vacuum deployment and testing of a 20m solar sail system," in 47th AIAA/ASME/ASCE/AHS/ASC Structures, Structural Dynamics, and Materials Conference, (Newport, Rhode Island), May 2006. Paper No. AIAA-2006-1705.

[29] Y. Tsuda, O. Mori, R. Funase, H. Sawada, T. Yamamoto, T. Saiki, T. Endo, and J. Kawaguchi, "Flight status of IKAROS deep space solar sail demonstrator," in 61st International Astronautical Congress, (Prague, Czech Republic), September 2010. Paper No. IAC-10-A3.6.8.

[30] C. Adams. Technical communications, 6 August 2008.

[31] L. D. Freidman, "LightSail: A new way and a new chance to fly on light." [Website, accessed 12 November 2010], http://www.planetary.org/programs/projects/solar sailing/tpr lightsail.html, 2011.

[32] B. Wie, "Solar sail attitude dynamics and control, part 1," *J. Guid. Control, Dyn*., vol. 27, pp. 526-535, July-August 2004.

[33] R. Burton, V. Coverstone, J. Hargens-Rysanek, K. Ertmer, T. Botter, G. Benavides, B. Woo, D. Carroll, P. Gierow, G. Farmer, and J. Cardin, "Ultrasail - ultra-lightweight solar sail concept," in AIAA/ASME/SAE/ASEE Joint Propulsion Conference and Exhibit, July 2005.

[34] R. Funase, O. Mori, Y. Tsuda, Y. Shirasawa, T. Saiki, Y. Mimasu, and J. Kawaguchi, "Attitude control of IKAROS solar sail spacecraft and its flight results," in 61st International Astronautical Congress, (Prague, Czech Republic), September 2010. Paper No. IAC-10-C1.4.3.

[35] B. Wie, "Solar sail attitude dynamics and control, part 2," *J. Guid. Control, Dyn.*, vol. 27, pp. 536-544, July-August 2004.

[36] M. Polites, J. Kalmanson, and D. Mangus, "Solar sail attitude control using small reaction wheels and magnetic torquers," *Proc. Inst. Mech. Eng. Part G: J. Aerosp. Eng*., vol. 222, no. 1, pp. 53-62, 2008.

[37] H. W. Price, J. Ayon, C. Garner, G. Klose, E. Mettler, and G. Sprague, "Design for a solar sail demonstration mission," in Space Technology and Applications International Forum (STAIF-2001), (Albuquerque, New Mexico), February 2001.

[38] B. Wie and D. Murphy, "Solar-sail attitude control design for a sail flight validation mission," *J. Spacecr. Rocket*., vol. 44, pp. 809-821, July-August 2007.

[39] C. Scholz, D. Romagnoli, and B. Dachwald, "Performance analysis of an attitude control system for solar sails using sliding masses," in 2nd International Symposium on Solar Sailing, New York City College of Technology, City University of New York, (Brooklyn, New York), pp. 171-176, July 2010.

[40] M. Nehrenz, A. Diaz, T. Svitek, and C. Biddy, "Initial design and simulation of the attitude determination and control system for LightSail-1," in 2nd International Symposium on Solar Sailing, New York City College of Technology, City University of New York, (Brooklyn, New York), pp. 135-140, July 2010.

[41] A. Pukniel, V. Coverstone, J. Warner, and R. Burton, "A preliminary study of the dynamics and control of the CubeSail spacecraft," *Adv. Astronaut. Sci*., vol. 135, pp. 1929-1948, August 2009.

[42] A. Pukniel, V. Coverstone, R. Burton, and D. Carroll, "Attitude control of the CubeSail solar sailing spacecraft in low Earth orbit," in 2nd International Symposium on Solar Sailing, New York City College of Technology, City University of New York, (Brooklyn, New York), pp. 121-126, July 2010.

[43] G. G. Wawrzyniak and K. C. Howell, "Trajectory control for a solar sail spacecraft in an offset lunar orbit," in 61st International Astronautical Congress, (Prague, Czech Republic), September 2010. Paper No. IAC-10.C1.2.3.

[44] B. Dachwald, M. Macdonald, C. R. McInnes, G. Mengali, and A. A. Quarta, "Impact of optical degradation on solar sail mission performance," *J. Spacecr Rocket*, vol. 44, pp. 740-749, July-August 2007.

Received: February 26, 2011 Revised: June 29, 2011 Accepted: September 10, 2011